Strong Dzyaloshinskii-Moriya interaction in two-dimensional magnets via lithium absorption

Cheng Ma [1,2] Kuijuan Jin [1,2,3,*] Chen Ge [1,2] Er-Jia Guo [1,2] Can Wang [1,2,3] and Xiulai Xu [1,4]

[1] *Institute of Physics, Chinese Academy of Sciences, Beijing 100190, China*
[2] *University of Chinese Academy of Sciences, Beijing 100049, China*
[3] *Songshan Lake Materials Laboratory, Dongguan, Guangdong 523808, China*
[4] *State Key Laboratory for Mesoscopic Physics and Frontiers Science Center*
for Nano-optoelectronics, School of Physics, Peking University, Beijing 100871, China

Dzyaloshinskii-Moriya interaction (DMI) is of particular interest as it plays a primary role in stabilizing topological chiral magnetism such as skyrmions and has been intensively studied due to its potential applications for next-generation information storage technologies. For two-dimensional (2D) magnets, although Janus structure offers a paradigm to realize strong DMI, further studies are confined by the strict fabrication and the necessity of heavy atoms. Here, using first-principles calculations, we propose a strategy beyond this limit, where Li atoms are absorbed on the surface of a 2D magnet, resulting in a strong DMI through the Rashba effect by introducing an effective electric field generated by the perpendicular electronic polarization due to the charge transfer after the absorption. Furthermore, taking $MnSe_2$ monolayer as an example, we predict the various phase transitions of skyrmions under strain manipulations and external magnetic fields. Our findings pave a road toward obtaining topological chiral magnetism.

I. INTRODUCTION

Topological chiral magnetic structures such as magnetic skyrmions are intensively studied due to their fundamental importance for magnetic interactions and potential applications for next-generation information storage technologies [1–5]. Stabilizing skyrmions basically relies on the coaction of the exchange interaction which aligns the neighboring spins, the Dzyaloshinskii-Moriya interaction (DMI) which tilts them, the magnetic anisotropy which determines the energetically preferred orientations, and the long-range dipolar interaction in thin-film systems [6,7]. However, the DMI is generally much weaker as it arises from the spin-orbital coupling (SOC) in noncentrosymmetric systems [8]. Therefore, much effort has been devoted to ferromagnet/heavy-metal heterostructures and multilayers on account of the strong SOC in heavy metals. For example, the atomic-scale skyrmion lattice was first observed in Fe monolayer on Ir(111) surface at low temperature [1]. Subsequently, individual skyrmions at room temperature were observed in the Ir/Co/Pt and Ir/Fe/Co/Pt multilayers where the ferromagnet layers were sandwiched by two different heavy metals [2,6].

Meanwhile, two-dimensional (2D) magnets such as CrI_3, Fe_3GeTe_2, and $MnSe_2$ monolayers offer promising opportunities to reduce the size of spintronics devices down to extremely small thickness [9–11]. Constructing Janus structures based on these 2D magnets has been proposed to induce strong DMI through breaking the spatial inversion symmetry and introducing heavy atoms [12–15]. Although a number

of Janus monolayers have been experimentally fabricated, it remains a challenge to synthesize them indiscriminately [16–18]. Therefore, it has been immensely desired to bring forward new strategies with more experimental feasibility. On the other hand, Yang *et al.* argued that ferromagnetic (FM) metal thin films coated by light atoms such as Co/graphene and Ni/graphene heterostructures can also manifest remarkable DMI due to the Rashba effect [19]. Subsequently, several studies reveal that FM metal thin films coated by other light atoms or nonmagnetic van der Waals materials exhibit strong DMI as well, confirming the feasibility of inducing strong DMI through the Rashba effect [20–26], which was proposed theoretically even earlier [27,28]. Motivated by these works, we explore the possibility to induce strong and intrinsic DMI in 2D magnets beyond the traditional paradigm.

In this work, we propose a strategy giving rise to strong DMI in 2D magnets by absorbing Li atoms on the top surface, which has been widely adopted to modulate the electronic structures [29–32]. Taking $MnSe_2$ monolayer as an example, which exhibits the ferromagnetism at room temperature [11], we address the energetically favorable absorption position by considering two potential ones and confirm the dynamical stability of the lithium-absorbed $MnSe_2$ ($MnSe_2$-Li) monolayer from its phonon spectrum. It is found that the Li atoms are bound with the neighboring Se atoms and the electrons transfer downwards in general after the absorption. Then, we investigate the in-plane DMI and obtain a large DMI vector, which is comparable with those in the state-of-art systems. To understand the surprisingly prominent DMI strength since the heavy atoms are absent, we calculate the average local potential of $MnSe_2$-Li monolayer along the out-of-plane direction and find a large difference of the vacuum level between

*kjjin@iphy.ac.cn

the top and the bottom surfaces, which can be effectively considered as a perpendicular electric field, leading to the strong Rashba effect and inducing the strong DMI. To confirm this, we calculate the band structures of $MnSe_2$-Li monolayers with two opposite in-plane spin directions and find the subelectronvolt-scale Rashba-type splitting. Furthermore, we perform the micromagnetic simulations to find the possible chiral magnetic structures for this specific case under strain manipulations and external magnetic fields by considering the DMI, the Heisenberg isotropic exchange interaction, the magnetic single-ion anisotropy, the demagnetization effect, and the Zeeman effect. Consequently, we find that most skyrmion phases are allowed to be stabilized in $MnSe_2$-Li monolayer including individual skyrmions (IS), square skyrmion crystals (SSC), and rhombic skyrmion crystals (RSC). Our work provides a strategy to design 2D magnets with strong DMI in a more low-cost and flexible way.

II. COMPUTATIONAL METHODS

Our first-principles calculations are based on density-functional theory (DFT) as implemented in the Vienna *Ab initio* Simulation Package [33,34], using the projector augmented-wave method [35]. The exchange-correlation potential is adopted by the generalized gradient approximation of the Perdew-Burke-Ernzerhof functional [36]. The DFT+U method [37,38] is adopted to improve the description of on-site Coulomb interactions of the Mn-3d orbitals with the effective U_{eff} set as 3.9 eV [15,39]. The van der Waals correction is considered using the DFT-D3 method with Becke-Johnson damping function [40,41]. The plane-wave cutoff energy is set to 520 eV. Γ-centered $\boldsymbol{k}$ meshes of $20 \times 20 \times 1$, $10 \times 20 \times 1$, and $5 \times 20 \times 1$ are adopted for unit cell, 2×1 supercell, and 4×1 supercell, respectively. The lattice parameters and the ionic positions are fully optimized until the forces on the ions are less than 10^{-3}eV/Å. The energy convergence criterion is set to be 10^{-6} eV. A vacuum with the thickness above 10 Å is built to avoid artificial interactions between periodic images. The phonon spectrum is calculated using the finite displacement method as implemented in the PHONOPY package [42]. The micromagnetic simulations are performed using the MUMAX3 package [43].

III. RESULTS AND DISCUSSION

A. Geometric properties and lithium absorption

$MnSe_2$ monolayer, a typical case of $1T$ (one-layer stack in the tetragonal symmetry) phase transition-metal dichalcogenides, harbors a hexagonal lattice with spatial inversion symmetry [11]. Upon the surface of $MnSe_2$ monolayer, which is composed of Se atoms arranged in hexagons, two potential absorption positions (labeled as P1 and P2) locate on the center of three neighbored Se atoms as shown in Fig. 1(a). To find out the energetically favored absorption position, we calculate the absorption energies for P1 and P2, which are defined as $E_{\text{abs}} = E_{MnSe_2\text{-Li}} - E_{MnSe_2} - E_{\text{Li}}$, where $E_{MnSe_2\text{-Li}}$ represents the energies of $MnSe_2$-Li monolayers with two absorption positions, E_{MnSe_2} represents the energy of $MnSe_2$ monolayer, and E_{Li} represents the energy of an isolated Li atom in a $10 \times 10 \times 10$ Å^3 vacuum box [44,45]. The E_{abs} thus
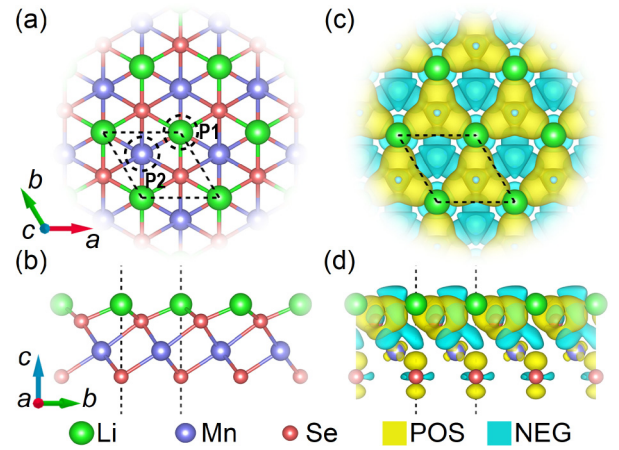

FIG. 1. (a) Top view and (b) side view for structure of $MnSe_2$-Li monolayer. Two potential absorption positions (P1 and P2) are circled by dashed lines and unit cell is framed by dashed lines. (c) Top view and (d) side view for charge-density difference ρ_{diff} with yellow patches for positive (POS) values and blue patches for negative (NEG) values.

denotes the energy required for $MnSe_2$ monolayer to absorb an Li atom per unit cell. The obtained E_{abs} for P1 and P2 are -3.12 and -3.06 eV, respectively, suggesting that the lithium absorption in both P1 and P2 are energetically allowed and the P1 is preferred. Given that, we only take the $MnSe_2$-Li monolayer with the absorption position P1 into our concern. Consequently, the equilibrium crystal structure of $MnSe_2$-Li monolayer, as shown in Figs. 1(a) and 1(b), belongs to a space group $P3m1$ with the lattice constants $a = b = 3.81$ Å, which is larger than that of the $MnSe_2$ monolayer due to the additional electrons taken from the absorbed Li atoms. To analyze the charge transfer and the bonding method between the Li atoms and the $MnSe_2$ monolayer, the charge-density difference ρ_{diff} is calculated using the first-principles calculations. Herein, the ρ_{diff} is defined as $\rho_{\text{diff}} = \rho_{MnSe_2\text{-Li}} - \rho_{MnSe_2} - \rho_{\text{Li}}$, where $\rho_{MnSe_2\text{-Li}}$ represents the charge density of $MnSe_2$-Li monolayer, while ρ_{MnSe_2} and ρ_{Li} represent that of the intercepted $MnSe_2$ monolayer and Li atomic layer, respectively. Therefore, the positive ρ_{diff} indicates electron density increase after lithium absorption and the negative ρ_{diff} denotes the electron density decrease. As illustrated in Figs. 1(c) and 1(d), the electrons gather among the Li atoms and their three nearest-neighboring Se atoms, indicating the strong binding of them. Besides, it is worth noting that the electrons transfer downwards in general, exhibiting an out-of-plane electronic polarization. Then, to check the stability of the $MnSe_2$-Li monolayer, the phonon spectrum is calculated and shows nearly no negative frequency throughout the Brillouin zone, indicating its dynamical stability (see Fig. S1 in Supplemental Material [46]; see also Refs. [43,47] therein).

B. DMI and other magnetic properties

Afterwards, we consider the following Hamiltonian to describe the magnetic interactions for the spins of Mn atoms in
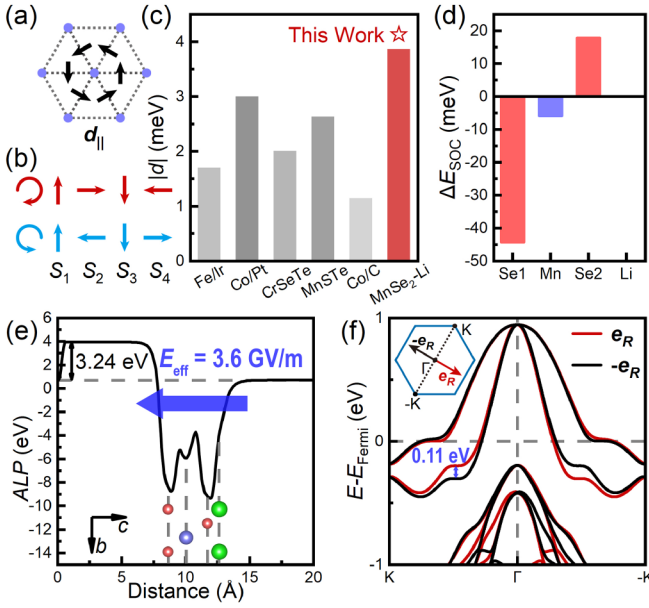
FIG. 2. (a) Diagram for in-plane DMI component $d_\parallel$ between nearest-neighboring Mn atomic pairs. (b) Magnetic configurations for 4×1 supercells of MnSe$_2$-Li monolayer, where red arrows represent CW spin spiral configuration while the blue arrows represent CCW one. (c) Comparison of magnitudes of $|d|$ for Fe/Ir(111), Co/Pt thin films, CrSeTe, MnSTe Janus monolayers, Co/graphene bilayer, and MnSe$_2$-Li monolayer. (d) Atom-layer resolved localization of DMI associated SOC energy ΔE_{SOC}, where bottom and top layers of Se atoms are labeled as Se1 and Se2, respectively. (e) Average local potential (ALP) along axis c. (f) Band structures of MnSe$_2$-Li monolayer from K (1/3, 1/3, 0) to $-K$ ($-1/3$, $-1/3$, 0) with spin directions along e_R and $-e_R$, respectively. Inset diagram demonstrates two opposite spin directions.

the hexagonal lattice:

$$H_{mag} = -\sum_{\langle i,j \rangle} d_{ij} \cdot (S_i \times S_j) - J \sum_{\langle i,j \rangle} S_i \cdot S_j$$
$$-K \sum_i (S_i^z)^2, \tag{1}$$

where S_i and S_j represent the unit spin vectors on the site i and j respectively, $\langle i, j \rangle$ refers to the nearest-neighboring Mn atomic pairs, and S_i^z is the z component of S_i. The DMI, the Heisenberg isotropic exchange, and the magnetic single ion anisotropy are characterized by the parameters d_{ij}, J, and K in the corresponding terms, respectively.

First, the DMI in the MnSe$_2$-Li monolayer is investigated. Given that a mirror plane exists perpendicular to the displacement vector e_{ij} of the nearest-neighboring Mn atomic pair and passes through their midpoint, the DMI vector d_{ij} can be expressed as $d_{ij} = d_\parallel (z \times e_{ij}) + d_\perp z$, where z is the unit vector of the axis z [see Fig. 2(a)], according to Moriya's symmetry rules [48]. Here, we do not take the $d_\perp$ into account as its contribution to stabilize skyrmions is negligible. The $d_\parallel$ is derived from our first-principles calculations by setting a clockwise (CW) spin spiral configuration and a counterclockwise (CCW) spin spiral configuration on the 4×1 supercells

[12,13,15,49] [see Fig. 2(b)]:

$$CW : S_1 = (0, 0, 1), S_2 = (1, 0, 0), S_3 = (0, 0, -1),$$
$$S_4 = (-1, 0, 0),$$
$$CCW : S_1 = (0, 0, 1),$$
$$S_2 = (-1, 0, 0), S_3 = (0, 0, -1), S_4 = (1, 0, 0).$$
$$\tag{2}$$

The energy difference between them is contributed by the DMI. Consequently, we can obtain (see Supplemental Material for details [46])

$$d_\parallel = (E_{CCW} - E_{CW})/12, \tag{3}$$

where E_{CCW} and E_{CW} represent the energies of the 4×1 supercells with CCW spin spiral and CW spin spiral configurations, respectively, and $d_\parallel > 0$ denotes the energetically favorable CW spin spiral, and $d_\parallel < 0$ indicates just the contrary. Surprisingly, the $d_\parallel$ of the MnSe$_2$-Li monolayer turns out to be 3.87 meV, which is even larger than those in a number of state-of-art systems such as Fe/Ir(111) (1.7 meV) [50], Co/Pt (3 meV) [51] heterostructures, CrSeTe (2.01 meV) [12], MnSTe (2.63 meV) [13] Janus monolayers, and Co/graphene (1.14 meV) [19] bilayer [see Fig. 2(c)]. To explore the origin of this unexpected large DMI vector since the heavy atoms are absent in the MnSe$_2$-Li monolayer, we check the atomic resolved localization of the DMI-associated SOC energy ΔE_{SOC}, which is defined as the SOC energy difference between CW and CCW spin spiral configurations [15]. As shown in Fig. 2(d), the main contribution to the ΔE_{SOC} is donated by the bottom Se atoms rather than the top ones who absorb the Li atoms, suggesting that the mechanism of the DMI can hardly be simply explained by the interfacial DMI under the Fert-Lévy model [52].

Subsequently, we calculate the average local potential of the MnSe$_2$-Li monolayer along the axis c ($\sim z$) with the dipole correction adopted [53]. As shown in Fig. 2(e), the vacuum level of the bottom surface is higher than that of the top surface by 3.24 eV. Considering the distance between the two energy steps as 9 Å, an effective electric field E_{eff} of 3.6 GV/m can be extracted. Taking advantage of the E_{eff}, we are able to understand the strong DMI through the SOC. As is well known, the Pauli SOC term is

$$H_{SOC} = -\frac{\hbar}{4m_0^2 c^2} \sigma \cdot p \times (\nabla V_0), \tag{4}$$

where $\hbar$ is the Planck constant, m_0 is the mass of a free electron, c is the velocity of light, p is the momentum operator, V_0 is the Coulomb potential, and $\sigma = (\sigma_x, \sigma_y, \sigma_z)$ is the vector of Pauli spin matrices [54]. Due to the absorption of Li atoms on only the top side, the Rashba-type SOC (RSOC) term can be obtained:

$$H_{Rashba} = \alpha_R \sigma \cdot (p \times z), \tag{5}$$

where $\alpha_R = -\frac{\hbar E_{local}}{4m_0^2 c^2}$ characterizes the strength of RSOC and the local electric field E_{local} should be positively correlated with the E_{eff}. According to the previous literature [8,27,28], the DMI can be induced through the Rashba effect:

$$D = 2 \frac{2\alpha_R m_0}{\hbar^2} A, \tag{6}$$

TABLE I. Crystal and magnetic parameters of $MnSe_2$ and $MnSe_2$-Li monolayers, including in-plane lattice constant a, magnetic moment per unit cell m, Heisenberg isotropic exchange parameter J, single-ion anisotropy parameter K, and in-plane DMI $d_\parallel$.

	a(Å)	$m(\mu_B)$	J(meV)	K(meV)	$d_\parallel$(meV)
$MnSe_2$	3.57	3.04	20.18	−0.57	
$MnSe_2$-Li	3.81	4.00	9.71	−3.80	3.87

where D and A refer to the micromagnetic parameters of DMI and exchange interactions, respectively.

To evaluate the strength of the Rashba effect in the $MnSe_2$-Li monolayer, we calculate the band structures with two opposite spin directions which are perpendicular to the K path and z [see the inset of Fig. 2(f)]. As is illustrated in Fig. 2(f), the subelectronvolt-scale Rashba-type splitting can be observed near the Fermi level, which suggests very strong RSOC owing to the significant E_{eff}.

As for the other magnetic parameters, the Heisenberg isotropic exchange parameter J is derived by mapping the results of our first-principles calculations onto the corresponding term in H_{mag} (see details in Supplemental Material [46]):

$$J = (E_{AFM} - E_{FM})/8, \tag{7}$$

where E_{AFM} and E_{FM} represent the energies of the 2×1 supercell with FM order and that with antiferromagnetic (AFM) order, respectively, and $J > 0$ denotes the FM coupling while $J < 0$ denotes the AFM coupling. Consequently, the calculated J for the $MnSe_2$-Li monolayer is 9.71 meV, which is smaller than that of the $MnSe_2$ monolayer (20.18 meV) (see Table I for the magnetic parameters of $MnSe_2$ and $MnSe_2$-Li monolayers). The magnetic single-ion anisotropy parameter K is derived from the difference between the energy with the spin direction [100] and that with the spin direction [001]:

$$K = E_{100} - E_{001}, \tag{8}$$

where $K > 0$ presents the perpendicular easy axis and $K < 0$ denotes the easy plane. Extraordinarily, the $MnSe_2$-Li monolayer manifests the easy plane with $K = -3.80$ meV, with the absolute value much larger than that of the $MnSe_2$ monolayer (−0.57meV). As a matter of fact, such strong in-plane single-ion anisotropy can be attributed to the Rashba effect as well. The RSOC term H_{Rashba} is identical to zero when the spin direction is perpendicular to the plane ($\sim z$). On the contrary, its magnitude reaches the maximum for an arbitrary electron with the momentum p when the spin direction is in the plane ($\sim z \times p$). Consequently, the magnetic anisotropy can be effectively manipulated when the Rashba effect is quite impactful [19,55,56].

Besides, the strain manipulation, as an effective way to modulate the physical properties (including the DMI) of materials, has been widely adopted in 2D materials owing to their high tolerability to strain [12,57,58]. Here, we probe the magnetic properties of the $MnSe_2$-Li monolayer under the in-plane biaxial strain ranging from −3% (compressive) to 3% (tensile). As demonstrated in Fig. 3(a), the magnitude of

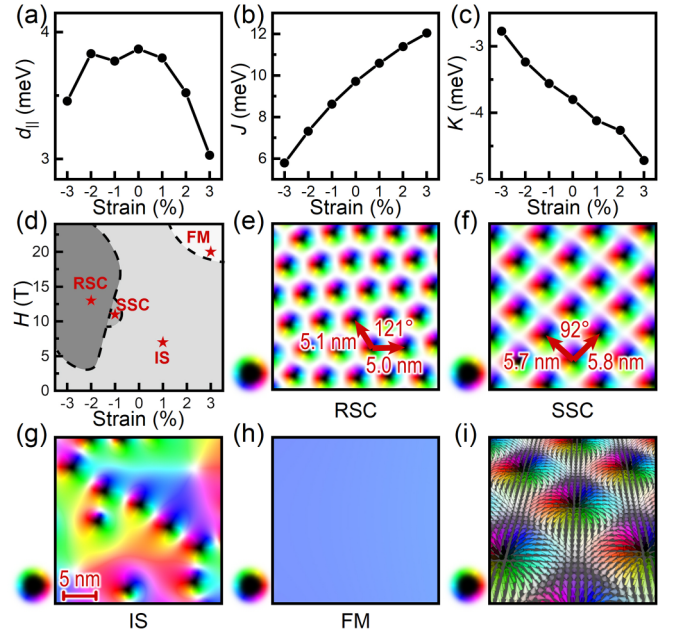FIG. 3. (a) In-plane DMI parameter $d_\parallel$, (b) Heisenberg isotropic exchange parameter J, and (c) magnetic single-ion anisotropy parameter K as function of biaxial strain ranging from −3 to 3%. (d) Skyrmion phase diagram including RSC, SSC, IS, and FM orders. (e) Partial (256×256) micromagnetic ground states of strained $MnSe_2$-Li monolayer with external magnetic fields, demonstrating RSC, (f) SSC, (g) IS, and (h) FM orders, respectively. (I) Spin configuration of SSC.

the $d_\parallel$ decreases with both the compressive and tensile strains, suggesting the maximum value near the equilibrium position. By contrast, the magnitudes of the J and the K increase with the tensile strains and decrease with the compressive strains [see Figs. 3(b) and 3(c)].

C. Micromagnetic simulations

Furthermore, we explore the possibility of novel chiral magnetic structures in the $MnSe_2$-Li monolayer under the uniform external magnetic field $\boldsymbol{H}(\boldsymbol{r}) = \boldsymbol{H}_0$ via micromagnetic simulations by considering the continuum total-energy functional of the unit local magnetization $\boldsymbol{M}(\boldsymbol{r})$:

$$E = E_{DMI}[\boldsymbol{M}(\boldsymbol{r})] + E_{ex}[\boldsymbol{M}(\boldsymbol{r})] + E_{ani}[\boldsymbol{M}(\boldsymbol{r})] + E_{dem}[\boldsymbol{M}(\boldsymbol{r})]$$
$$+ E_{Zeeman}[\boldsymbol{M}(\boldsymbol{r}), \boldsymbol{H}(\boldsymbol{r})], \tag{9}$$

which includes the DMI, the exchange interaction, the magnetic single-ion anisotropy, the demagnetization effect (long-range interaction), and the Zeeman effect. The energy density of each specific term is given by [43]

$$\varepsilon_{DMI}(\boldsymbol{r}) = D(M_z(\nabla \cdot \boldsymbol{M}) - (\boldsymbol{M} \cdot \nabla)M_z),$$
$$\varepsilon_{ex}(\boldsymbol{r}) = A(\nabla \boldsymbol{M})^2,$$
$$\varepsilon_{ani}(\boldsymbol{r}) = -K_u(M_z)^2,$$
$$\varepsilon_{dem}(\boldsymbol{r}) = -\frac{1}{2}M_s\boldsymbol{M} \cdot \boldsymbol{B}_{dem}$$
$$\varepsilon_{Zeeman}(\boldsymbol{r}) = -M_s\boldsymbol{M} \cdot \boldsymbol{H}, \tag{10}$$

where M_s refers to the saturation magnetization, M_z refers to the z component of the local magnetization, and $\boldsymbol{B}_{\mathrm{dem}}(\boldsymbol{r}) = -\frac{1}{4}\int_V \nabla\nabla\frac{1}{|\boldsymbol{r}-\boldsymbol{r}'|}\cdot\boldsymbol{M}(\boldsymbol{r}')d\boldsymbol{r}'$ refers to the demagnetizing field [59], respectively. The parameters D, A, K_u, and M_s are the magnetic parameters applicable to the continuum model, corresponding to the $d_\parallel$, J, K, and m, respectively. The relationship between each two of them can be derived by mapping the discrete model to the continuum one with the specific lattice structure (see Supplemental Material for details [46]):

$$D = -\frac{\sqrt{3}d_\parallel}{at}, \quad A = \frac{\sqrt{3}J}{2t}, \quad K_u = \frac{2K}{\sqrt{3}a^2t}, \quad M_s = \frac{2m}{\sqrt{3}a^2t},$$
(11)

where $t = 7\text{Å}$ represents the effective thickness of the MnSe$_2$-Li monolayer.

Moreover, our micromagnetic simulations are performed on the $1024\times 1024\times 1$ supercells where the size of each unit cell is set as $0.1\text{nm}\times 0.1\text{nm}\times t$ to conduct the numerical calculations. The in-plane periodic boundary conditions are adopted to reduce the influence of the finite size of the supercell. To be noted, the unit cells in the micromagnetic simulations are arranged in square, leading to a square geometry which may slightly influence the final results. We perform micromagnetic simulations with random initial states and add a simulated annealing from 200 K down to 0 K before energy minimization.

Consequently, the magnetic structure phase diagram of the MnSe$_2$-Li monolayer can be plotted as shown in Fig. 3(d), including the RSC, the SSC, the IS, and the FM orders. To be noted, some of these skyrmion states are actually metastable states concluded from the micromagnetic simulations with uniform initial states [all spins align along (1,1,0)] and some final states (FM states) with even lower total energies (see Figs. S12 and S13). Nevertheless, these metastable skyrmion states are actually easier to get as long as the initial states is set randomly or the annealing process is performed before energy minimization due to the topological stability of skyrmions, i.e., once the skyrmions are formed, it will be difficult to overcome the energy barriers and turn to the FM state even though the FM state is energetically preferred. We also reperform the micromagnetic simulations with different conditions (without periodic boundary conditions or with rectangular supercells) to ensure our results (see Figs. S14 and S15).

Under proper external magnetic field, the skyrmion states become energetically preferred and the close-packed RSC phase arises since the rhombic lattice allows the maximum density of skyrmions. As one can expect, with the external magnetic field getting stronger, the RSC phase becomes sparser and turns to FM state eventually. On the other hand, our results, in which the in-plane anisotropy was not considered during the micromagnetic simulations, suggest that the SSC phase might occur as a metastable state (see Fig. S13) in a very limited range [see Fig. 3(d)]. To be noted, the SSC phase, as far as we know, was mostly reported in tetragonal rare-earth based centrosymmetric itinerant magnets originated from the four-spin interaction mediated by itinerant electrons [3,60–63], whereas the possibility of stabilizing SSC phase through the mechanism of DMI is not widely discussed. Therefore, further investigations about this issue are highly expected.
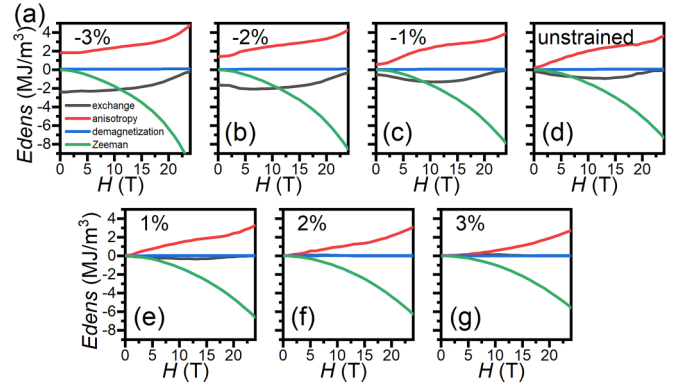

FIG. 4. Energy densities of exchange interaction (including DMI), anisotropy, demagnetization effect, and Zeeman effect for micromagnetic simulation results of MnSe$_2$-Li monolayers [strained from $-3 \sim 3\%$, (a)~(g)] under external magnetic fields (0~24 T).

The representative cases of each phase are marked by stars and the partial (256×256) micromagnetic results of each of them are shown in Figs. 3(e), 3(f), 3(g), and 3(h), respectively (more details are available in Supplemental Material [46]). The nanometer-scale skyrmions that emerged [also shown in Fig. 3(i)] are promising for the application of extremely high-density memories and the phase transitions are of great importance for basic physics to understand the magnetic interactions as well. However, the skyrmion crystal phases in the MnSe$_2$-Li monolayer require large external magnetic fields, which is not beneficial to the experimental verification. The dominating factor for that is the strong in-plane magnetic anisotropy as the magnetic anisotropy energy in skyrmions costs so much that a large external magnetic field is demanded to balance it, which is also consistent with the earlier reports [56]. Therefore, further theoretical and experimental studies are intensely expected to seek for more proper candidates along the way we suggested here.

In addition, we extract the energy densities of the total exchange interaction (including the symmetric exchange interaction and the antisymmetric one, i.e., the DMI, as they are calculated together by MUMAX3), the anisotropy, the Zeeman effect, and the demagnetization effect as shown in Fig. 4. The Zeeman energy density increases nonlinearly with the increase of external magnetic field, suggesting the nonlinearly increase of M_z. The anisotropy energy density increases from two aspects: the nonlinearly increasing M_z and the formation of chiral states (including the skyrmion states). Therefore, the anisotropy energy density in 3% strained MnSe$_2$-Li monolayer increases more smoothly due to less formation of chiral states. The total exchange-energy density is mainly contributed by the symmetric exchange interaction and the DMI, in which the former increases with the formation of chiral states while the latter decreases with it. The competition between these two interactions and the formation of chiral states result in the complex curves in Fig. 4. Last but not least, the demagnetization energy density is relatively small and only influences the results slightly in these cases.

IV. CONCLUSION

In this work, we have proposed a strategy to induce strong DMI in 2D magnets going beyond the limit of heavy atoms and Janus structures, where Li atoms are absorbed on the surface of a 2D magnet and therefore induce the DMI through the Rashba effect by introducing the effective electric field E_{eff} generated by the perpendicular electronic polarization due to the charge transfer after the lithium absorption. Taking the $MnSe_2$ monolayer as an example, we demonstrated the mechanism of this strong DMI through the first-principles calculations. Furthermore, the potential chiral magnetic structures in this specific case were discovered via the micromagnetic simulations and the magnetic structure phase diagram was plotted where the skyrmions harbor a nanometers-scale size, shedding some light on the application of extremely high-density memories.

More importantly, the Janus monolayers, MoSSe monolayers for example, are mainly obtained by the sulfurization of only one side of Se atoms [17,18]. This process was conducted in a chemical vapor deposition device under relatively higher temperatures due to the replacement of Se atoms by S atoms needing an energy to break the chemical bond first, which also brought more uncertainty, i.e., the S atoms might diffuse to the other side and sulfurize both sides of $MoSe_2$ monolayers. On the contrary, the lithium absorption on the surface of 2D magnets presented in this paper can be easily achieved by molecular-beam epitaxy or lithium-ion liquid regulation under much lower temperatures, providing a low-cost, reliable, and flexible way that can be applied on an arbitrary 2D magnet without considering the heavy metals or overcoming the nodus of fabricating Janus monolayers. Besides, the absorption rate of Li atoms, the external electric field, and even the absorption elements are all potential manipulation ways that should effectively modulate the magnetic properties of the absorbed 2D magnets. We believe that our findings provide a way to obtain topological chiral magnetism in 2D materials.

[1] S. Heinze, K. von Bergmann, M. Menzel, J. Brede, A. Kubetzka, R. Wiesendanger, G. Bihlmayer, and S. Blügel, Nat. Phys. **7**, 713 (2011).

[2] C. Moreau-Luchaire, C. Moutafis, N. Reyren, J. Sampaio, C. A. F. Vaz, N. Van Horne, K. Bouzehouane, K. Garcia, C. Deranlot, P. Warnicke *et al.*, Nat. Nanotechnol. **11**, 444 (2016).

[3] R. Takagi, N. Matsuyama, V. Ukleev, L. Yu, J. S. White, S. Francoual, J. R. L. Mardegan, S. Hayami, H. Saito, K. Kaneko *et al.*, Nat. Commun. **13**, 1472 (2022).

[4] B. Ding, Z. Li, G. Xu, H. Li, Z. Hou, E. Liu, X. Xi, F. Xu, Y. Yao, and W. Wang, Nano Lett. **20**, 868 (2020).

[5] J. Liang, Q. Cui, and H. Yang, Phys. Rev. B **102**, 220409(R) (2020).

[6] A. Soumyanarayanan, M. Raju, A. L. Gonzalez Oyarce, A. K. C. Tan, M.-Y. Im, A. P. Petrović, P. Ho, K. H. Khoo, M. Tran, C. K. Gan *et al.*, Nat. Mater. **16**, 898 (2017).

[7] J. Lucassen, M. J. Meijer, O. Kurnosikov, H. J. M. Swagten, B. Koopmans, R. Lavrijsen, F. Kloodt-Twesten, R. Frömter, and R. A. Duine, Phys. Rev. Lett. **123**, 157201 (2019).

[8] A. Kundu and S. Zhang, Phys. Rev. B **92**, 094434 (2015).

[9] B. Huang, G. Clark, E. Navarro-Moratalla, D. R. Klein, R. Cheng, K. L. Seyler, D. Zhong, E. Schmidgall, M. A. McGuire, D. H. Cobden *et al.*, Nature (London) **546**, 270 (2017).

[10] Y. Deng, Y. Yu, Y. Song, J. Zhang, N. Z. Wang, Z. Sun, Y. Yi, Y. Z. Wu, S. Wu, J. Zhu *et al.*, Nature (London) **563**, 94 (2018).

[11] D. J. O'Hara, T. Zhu, A. H. Trout, A. S. Ahmed, Y. K. Luo, C. H. Lee, M. R. Brenner, S. Rajan, J. A. Gupta, D. W. McComb *et al.*, Nano Lett. **18**, 3125 (2018).

[12] Q. Cui, J. Liang, Z. Shao, P. Cui, and H. Yang, Phys. Rev. B **102**, 094425 (2020).

[13] J. Liang, W. Wang, H. Du, A. Hallal, K. Garcia, M. Chshiev, A. Fert, and H. Yang, Phys. Rev. B **101**, 184401 (2020).

[14] C. Xu, J. Feng, S. Prokhorenko, Y. Nahas, H. Xiang, and L. Bellaiche, Phys. Rev. B **101**, 060404(R) (2020).

[15] J. Yuan, Y. Yang, Y. Cai, Y. Wu, Y. Chen, X. Yan, and L. Shen, Phys. Rev. B **101**, 094420 (2020).

[16] R. Li, Y. Cheng, and W. Huang, Small **14**, e1802091 (2018).

[17] A. Y. Lu, H. Zhu, J. Xiao, C. P. Chuu, Y. Han, M. H. Chiu, C. C. Cheng, C. W. Yang, K. H. Wei, Y. Yang *et al.*, Nat. Nanotechnol. **12**, 744 (2017).

[18] J. Zhang, S. Jia, I. Kholmanov, L. Dong, D. Er, W. Chen, H. Guo, Z. Jin, V. B. Shenoy, L. Shi *et al.*, ACS Nano **11**, 8192 (2017).

[19] H. Yang, G. Chen, A. A. C. Cotta, A. T. N'Diaye, S. A. Nikolaev, E. A. Soares, W. A. A. Macedo, K. Liu, A. K. Schmid, A. Fert *et al.*, Nat. Mater. **17**, 605 (2018).

[20] G. Chen, A. Mascaraque, H. Jia, B. Zimmermann, M. Robertson, R. L. Conte, M. Hoffmann, M. A. G. Barrio, H. Ding, R. Wiesendanger *et al.*, Sci. Adv. **6**, eaba4924 (2020).

[21] G. Chen, M. Robertson, M. Hoffmann, C. Ophus, A. L. Fernandes Cauduro, R. Lo Conte, H. Ding, R. Wiesendanger, S. Blügel, A. K. Schmid *et al.*, Phys. Rev. X **11**, 021015 (2021).

[22] F. Ajejas, A. Gudin, R. Guerrero, A. Anadon Barcelona, J. M. Diez, L. de Melo Costa, P. Olleros, M. A. Nino, S. Pizzini, J. Vogel *et al.*, Nano Lett. **18**, 5364 (2018).

[23] A. Hallal, J. Liang, F. Ibrahim, H. Yang, A. Fert, and M. Chshiev, Nano Lett. **21**, 7138 (2021).

[24] J. Rastikian, S. Suffit, C. Barraud, A. Bellec, V. Repain, Y. Roussigné, M. Belmeguenai, S. Farhat, L. Le Laurent, C. Barreteau *et al.*, Phys. Rev. Mater. **5**, 014004 (2021).

[25] B. El-Kerdi, A. Thiaville, S. Rohart, S. Panigrahy, N. Brás, J. Sampaio, and A. Mougin, Nano Lett. **23**, 3202 (2023).

[26] P. Li, Q. Cui, Y. Ga, J. Liang, and H. Yang, Phys. Rev. B **106**, 024419 (2022).

[27] H. Imamura, P. Bruno, and Y. Utsumi, Phys. Rev. B **69**, 121303(R) (2004).

[28] K. W. Kim, H. W. Lee, K. J. Lee, and M. D. Stiles, Phys. Rev. Lett. **111**, 216601 (2013).

[29] K. M. O'Donnell, T. L. Martin, N. A. Fox, and D. Cherns, Phys. Rev. B **82**, 115303 (2010).

[30] D. T. Larson, S. Carr, G. A. Tritsaris, and E. Kaxiras, Phys. Rev. B **101**, 075407 (2020).

[31] E. Lee and K. A. Persson, Nano Lett. **12**, 4624 (2012).

[32] C. Li, L. Gu, X. Guo, D. Samuelis, K. Tang, and J. Maier, Nano Lett. **12**, 1241 (2012).

[33] G. Kresse and J. Hafner, Phys. Rev. B **49**, 14251 (1994).

[34] G. Kresse and J. Furthmu¨ller, Phys. Rev. B **54**, 11169 (1996).

[35] P. E. Blochl, Phys. Rev. B **50**, 17953 (1994).

[36] J. P. Perdew, K. Burke, and M. Ernzerhof, Phys. Rev. Lett. **77**, 3865 (1996).

[37] V. V. Anisimov, J. Zaanen, and O. K. Andersen, Phys. Rev. B **44**, 943 (1991).

[38] S. L. Dudarev, G. A. Botton, S. Y. Savrasov, C. J. Humphreys, and A. P. Sutton, Phys. Rev. B **57**, 1505 (1998).

[39] M. Kan, S. Adhikari, and Q. Sun, Phys. Chem. Chem. Phys. **16**, 4990 (2014).

[40] S. Grimme, J. Antony, S. Ehrlich, and H. Krieg, J. Chem. Phys. **132**, 154104 (2010).

[41] S. Grimme, S. Ehrlich, and L. Goerigk, J. Comput. Chem. **32**, 1456 (2011).

[42] A. Togo and I. Tanaka, Scr. Mater. **108**, 1 (2015).

[43] A. Vansteenkiste, J. Leliaert, M. Dvornik, M. Helsen, F. Garcia-Sanchez, and B. Van Waeyenberge, AIP Adv. **4**, 107133 (2014).

[44] B. Xu, L. Wang, H. J. Chen, J. Zhao, G. Liu, and M. S. Wu, Comput. Mater. Sci. **93**, 86 (2014).

[45] X. Tao, J. Wang, C. Liu, H. Wang, H. Yao, G. Zheng, Z. W. Seh, Q. Cai, W. Li, G. Zhou *et al.*, Nat. Commun. **7**, 11203 (2016).

[46] See Supplemental Material at http://link.aps.org/supplemental/10.1103/PhysRevB.108.134405 for (1) phonon spectrum; (2) derivation of the magnetic parameters; (3) magnetic parameters in continuum model; and (4) micromagnetic simulation results.

[47] T. M. H. Jin, *The Physics of Ferromagnetism*, Vol. 158 (Springer, 2012).

[48] T. Moriya, Phys. Rev. **120**, 91 (1960).

[49] H. Yang, J. Liang, and Q. Cui, Nat. Rev. Phys. **5**, 43 (2022).

[50] B. Dupe, M. Hoffmann, C. Paillard, and S. Heinze, Nat. Commun. **5**, 4030 (2014).

[51] H. Yang, A. Thiaville, S. Rohart, A. Fert, and M. Chshiev, Phys. Rev. Lett. **115**, 267210 (2015).

[52] A. Fert and P. M. Levy, Phys. Rev. Lett. **44**, 1538 (1980).

[53] J. Neugebauer and M. Scheffler, Phys. Rev. B **46**, 16067 (1992).

[54] R. Winkler, *Spin-Orbit Coupling Effects in Two-Dimensional Electron and Hole Systems*, Vol. 191 (Springer Berlin, Heidelberg, 2003).

[55] M. Vagadia, J. Sahoo, A. Kumar, S. Sardar, T. M. Tank, and D. S. Rana, Phys. Rev. B **107**, 064420 (2023).

[56] S. Banerjee, J. Rowland, O. Erten, and M. Randeria, Phys. Rev. X **4**, 031045 (2014).

[57] Z. Shen, C. Song, Y. Xue, Z. Wu, J. Wang, and Z. Zhong, Phys. Rev. B **106**, 094403 (2022).

[58] S. Qi, J. Jiang, X. Wang, and W. Mi, Carbon **174**, 540 (2021).

[59] A. Vansteenkiste and B. Van De Wiele, J. Magn. Magn. Mater. **323**, 2585 (2011).

[60] N. D. Khanh, T. Nakajima, X. Yu, S. Gao, K. Shibata, M. Hirschberger, Y. Yamasaki, H. Sagayama, H. Nakao, L. Peng *et al.*, Nat. Nanotechnol. **15**, 444 (2020).

[61] S. Hayami, Phys. Rev. B **105**, 174437 (2022).

[62] N. D. Khanh, T. Nakajima, S. Hayami, S. Gao, Y. Yamasaki, H. Sagayama, H. Nakao, R. Takagi, Y. Motome, Y. Tokura *et al.*, Adv. Sci. **9**, 2105452 (2022).

[63] M. Gen, R. Takagi, Y. Watanabe, S. Kitou, H. Sagayama, N. Matsuyama, Y. Kohama, A. Ikeda, Y. Ōnuki, T. Kurumaji *et al.*, Phys. Rev. B **107**, L020410 (2023).